PIER C

Design and Analysis of a Novel Dual-PM Flux-Reversal Machine with Halbach Array

Yeming Zhu, Longxiang Han, Mingji Yin, Yuhui Huang, and Libing Jing*

Hubei Provincial Engineering Technology Research Center for Microgrid
College of Electrical Engineering and New Energy, China Three Gorges University, Yichang 443002, China

ABSTRACT: Flux-reversing machines (FRMs) have the advantages of high torque density and wide speed range. However, their disadvantage is the low utilization rate of permanent magnets (PMs). To enhance PM utilization, a novel dual-PM FRM (DPFRM) with Halbach arrays is proposed in this paper. Halbach arrays are applied to both the stator interlayer and half of the rotor teeth, forming a consequent-pole structure together with iron cores. This layout significantly reduces the number of rotor magnets used. With the use of Halbach arrays, this design effectively reduces magnetic flux leakage. It also achieves higher torque density under low current conditions, demonstrating enhanced electromagnetic performance. To achieve better overall performance, both the conventional FRM and the proposed DPFRM are globally optimized. Their no-load and load performances are evaluated through finite element analysis (FEA). The analysis verifies that the DPFRM achieves higher back electromotive force (Back-EMF) and torque density, and also exhibits lower torque ripple. Therefore, the proposed design significantly improves PM utilization, effectively mitigating the primary limitation of conventional FRMs.

1. INTRODUCTION

With the advancement of rare-earth PM materials, PM machines have been widely applied due to their high torque density and energy efficiency [1]. Recent years have seen growing research efforts on high-performance PM machines through structural innovation and multiobjective optimization, such as the spoke-type axial-flux PM machine optimized for in-wheel drive operation [2], the dual three-phase permanent magnet synchronous hub motor designed using sequential subspace optimization [3], and the five-phase bearingless permanent magnet motor optimized with winding area constraints [4]. These studies demonstrate the potential of PM machines to achieve high torque density, improved efficiency, and reliable operation in demanding applications. However, conventional PM machines still face challenges such as increased volume and energy consumption under high torque demands. To address these issues, increasing attention has been directed toward flux modulation machines (FMMs) [5], which can be classified into rotor PM FMMs and stator PM FMMs according to the position of PM [6]. The rotor-PM topology offers inherently high torque density, which explains its industrial prevalence [7]. Nevertheless, excessive rotor temperature rise can cause irreversible PM demagnetization and limit power density, while stator-PM machines can mitigate this issue [8].

Stator PM motors include dual-striking PM (DSPM), flux-switching PM (FSPM), and FRM [9–11]. In a number of stator PM motors, FRM stands out because of its bipolar winding flux, which can produce high back-EMF and electromagnetic torque [12]. However, for the conventional FRM, about half

of the PMs in each working cycle will produce leakage flux, which makes the utilization efficiency of the magnet low [13]. In [14], a consequent-pole structure is proposed, in which half of the PMs are replaced with iron cores. In this design, the stator teeth act as "pole-pair modulators" linking the air-gap magnetic field with the stator magnetic field, thereby enhancing the main flux linkage and improving the utilization of the PMs. In [15], the rotor PM consequent-pole is introduced to form a DPFRM with the PM of the stator. Compared with the conventional FRM, the DPFRM demonstrates superior average torque, stronger overload tolerance, and higher operational efficiency, highlighting its suitability for direct-drive systems. In [16], the stator and rotor are improved to the consequent-pole structure, and the performances of the PM embedded in different positions of the stator tooth tip are compared. It is found that the stator topology with PM-Fe-PM-Fe sequence has higher back-EMF and torque density. In [13], a Halbach array is applied to the rotor PM while preserving the consequent-pole configuration in both stator and rotor. The rotor's Halbach arrays configuration enhances the magnetic field distribution in the air gap, enabling the generation of substantial torque while maintaining relatively low consumption of PM material. In [17], the stator PM is redesigned into a Halbach array while maintaining the consequent-pole configuration in both stator and rotor components. Both of them effectively reduce the flux leakage and improve the torque capacity.

In [18], a comparison is made between the hybrid excitation stator PM structure and dual-PM configuration. The results indicate that the dual-PM structure is more prone to magnetic saturation under DC excitation, while the stator PM with hybrid excitation exhibits a stronger flux regulation capability. In [19],

---

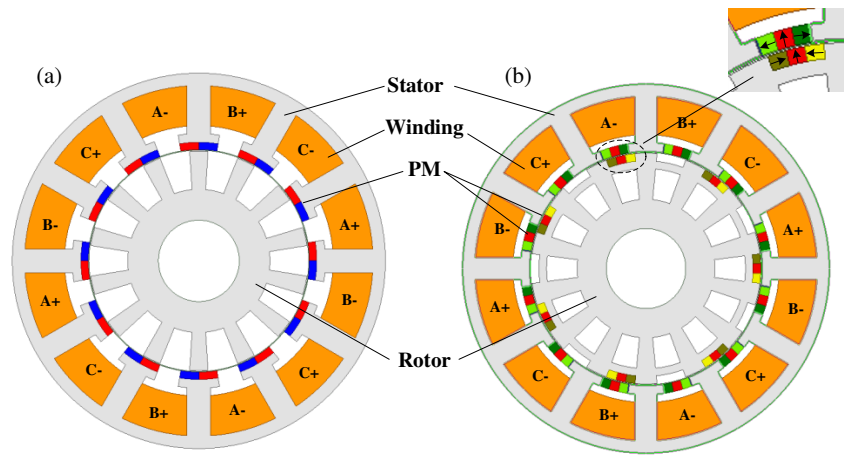* Corresponding author: Libing Jing (jinglibing163@163.com).

FIGURE 1. The topology of machines. (a) FRM. (b) DPFRM.

a comparison of the electromagnetic performances of four typical dual-PM machines is presented, including the double-stator PM (DSPM), stator multitooth-PM (SMTPM), stator slot PM (SSPM), and stator tooth PM (STPM). The results indicate that the STPM configuration effectively reduces magnetic flux leakage and achieves higher efficiency. In [20], the electromagnetic performances of four kinds of dual-winding dual-PM structures were compared. It was found that the performance of the stator and rotor with Halbach-array configuration was optimal. The use of distributed PM or auxiliary teeth can effectively reduce magnetic flux leakage, and the use of distributed PM can produce higher torque under overload conditions, that is, higher anti-demagnetization ability.

Although previous studies have introduced Halbach-array configuration into either the stator or rotor to enhance air-gap magnetic field, most designs have only employed Halbach arrays on a single side. Reports in which both the stator and rotor adopt Halbach configurations simultaneously are limited. Moreover, in the existing designs, the amount of PM material used in the rotor remains substantial, leading to higher material costs.

This paper proposes a novel DPFRM that features Halbach-array PMs on both the stator and rotor. The use of Halbach arrays improves magnetic flux concentration and significantly reduces leakage flux. Moreover, rotor PM usage is substantially reduced through selective placement, without compromising magnetic performance. Section 2 introduces the topologies and basic operating principles of DPFRM and FRM structures. Section 3 conducts global optimization to determine the optimal parameter sets. Sections 4 and 5 provide comparative analyses of their no-load and load performances. Finally, Section 6 summarizes the key findings and conclusions.

2. TOPOLOGY AND OPERATION PRINCIPLE

2.1. Topology

Figure 1 is a comparison of the structures of two topologies. In terms of structural parameters, the two motors are consistent: 12 stator slots are matched with 14 rotor poles, and the windings adopt the same two-pole configuration. The difference is that the DPFRM topology optimizes both the stator and rotor structures.

Compared with the conventional FRM stator, DPFRM adopts the PM of Halbach-array configuration in the stator and uses slots on both sides of the stator to clamp the PM. Each stator PM and its adjacent stator teeth will form a magnetic pole pair, making full use of the internal space. The conventional rotor only features a reluctance structure. The DPFRM rotor uses a Halbach-array PM configuration, forming a consequent-pole structure with the rotor core. The Halbach magnetization direction of the stator and rotor poles is marked in the upper right corner in Fig. 1(b).

2.2. Principle of Operation

For the DPFRM, the magnetic field should be analyzed by separating it into contributions from the stator, rotor, and PMs. The pole-pair rotational speed of the magnetic field produced by the stator and rotor PMs must match that of the field generated by the armature current. Beyond the fundamental component, harmonic components arise due to the asymmetrical distribution of magnetic reluctance. Harmonics that share identical pole-pair numbers and rotation speeds within the air gap can interact to produce electromagnetic torque [19].

The magnetomotive force (MMF) contributed by stator and rotor PMs in the DPFRM configuration can be mathematically formulated as follows:

$$F_s(\theta) = \sum_{i=1,3,5,...}^{\infty} F_{PMs} \cos(i P_{PMs} \theta) \quad (1)$$

where F_{PMs} is the corresponding Fourier coefficient, P_{PMs} the number of stator pole-pair, and θ the mechanical position in stationary coordinate.

$$F_r(\theta, t) = \sum_{j=1,2,3,...}^{\infty} F_{PMr} \cos(j P_{PMr}(\theta - \omega_r t)) \quad (2)$$
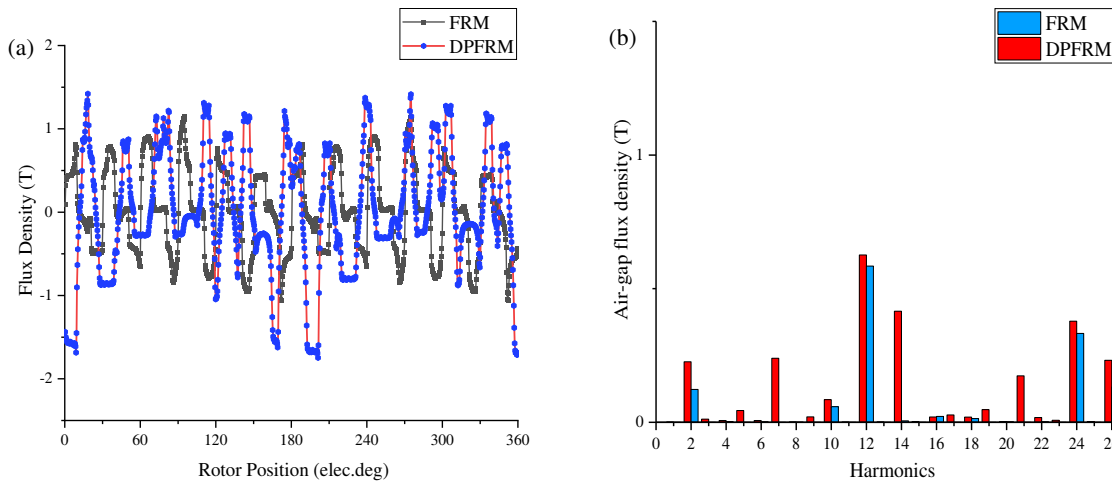
71

FIGURE 2. Radial air-gap flux density of FRM and DPFRM. (a) Waveform. (b) Harmonic spectra.

where F_{PMr} is the corresponding Fourier coefficient, P_{PMr} the number of rotor pole-pair, and ω_r the mechanical speed of the rotor.

The expression for the stator air-gap permeance can be formulated as follows:

$$\Lambda_s(\theta) = \sum_{v=0,1,2,...}^{\infty} \Lambda_s \cos(v N_s \theta) \tag{3}$$

where Λ_s is the corresponding Fourier coefficient, and N_s is the teeth number of the stator.

The rotor air gap permeance expression can be expressed as:

$$\Lambda_r(\theta, t) = \sum_{w=0,1,2,...}^{\infty} \Lambda_r \cos(w N_r(\theta - \omega_r t)) \tag{4}$$

where Λ_r is the corresponding Fourier coefficient, and N_r is the teeth number of the rotor.

Accordingly, the excitation flux density induced by the PMs on both the stator and rotor sides can be represented as follows:

$$B_{g\_s} = F_s(\theta) \cdot \Lambda_r(\theta, t)$$

$$= \sum_{i=1,3,5...}^{\infty} \sum_{w=0,1,2...}^{\infty} \frac{F_{PMs}\Lambda_r}{2}$$

$$\cos((wN_r \pm iP_{PMs})\theta - wN_r\omega_r t) \tag{5}$$

$$B_{g\_r} = F_r(\theta, t) \cdot \Lambda_s(\theta, t)$$

$$= \sum_{j=1,2,3...}^{\infty} \sum_{v=0,1,2...}^{\infty} \frac{F_{PMr}\Lambda_s}{2}$$

$$\cos((jP_{PMr} \pm vN_s)\theta - jP_{PMr}\omega_r t) \tag{6}$$

The harmonic characteristics of the single-layer and double-layer PM air-gap fields are presented in Table 1.

For the conventional FRM, the main working harmonics are 2nd, 12th, and 26th. According to Table 1, the 2nd and 26th harmonics can be obtained when $m = 1$, $n = 1$, and the 12th harmonics can be obtained when $m = 0$, $n = 1$. For the DPFRM

TABLE 1. Harmonic order expression of FRM and DPFRM.

|	Harmonic order	(m, n)
FRM	$\|mN_r \pm nN_s\|$	$m = 0, 1, 2, \ldots$
		$n = 1, 3, 5, \ldots$
DPFRM	$\|mN_r \pm nN_s\|$	$m = 0, 1, 2, \ldots$
		$n = 0, 1, 2, \ldots$

proposed in this paper, in addition to 2nd, 12th, and 26th as the main working harmonics, 7th, 14th, and 21th also contribute important output torque due to the 7-pair Halbach consequent-pole structure of the rotor.

Figure 2 illustrates the radial air-gap flux density of both the FRM and DPFRM, including its waveform and harmonic spectra. Besides the main working harmonics, many low-order harmonics are also synchronized and contribute to the generation of effective electromagnetic torque. These harmonics, together with the fundamental fields excited by the stator PM, rotor PM, and armature current, enhance torque production. Hence, the use of Halbach arrays in the dual-PM configuration not only increases the air-gap flux density but also enhances its harmonic richness, both of which contribute to improved torque production.

3. PARAMETER OPTIMIZATION DESIGN

The optimization process was conducted using MOGA (Multi-Objective Genetic Algorithm), a widely adopted evolutionary algorithm that efficiently addresses multiple conflicting objectives in engineering design. The overall procedure is illustrated in Fig. 3, and the fixed design and operating parameters for both the FRM and DPFRM are summarized in Table 2. Both motor structures were optimized using MOGA to achieve higher average torque and lower torque ripple for performance comparison, while keeping the current excitation, air gap length, and overall motor volume unchanged.

Figure 4 presents the sensitivity analysis results for the FRM and DPFRM. Key structural parameters of both machines are labeled in the figure for completeness. For FRM, the output
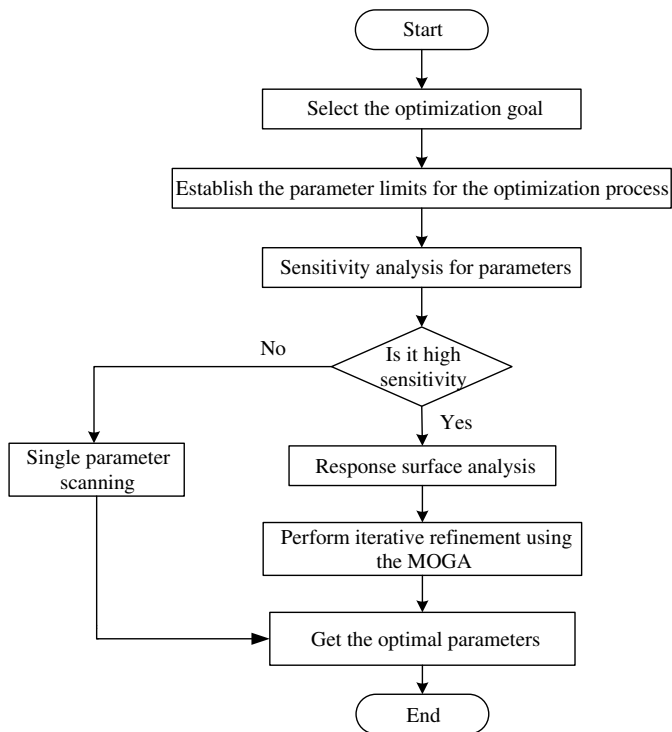
FIGURE 3. Flowchart of multi-objective optimization.

TABLE 2. Initial value of parameters.

Parameters	Value
Material of PM	NdFeB
Material of Iron	DW310-35
Axial length (mm)	60
Length of air gap (mm)	1
Stator outer radius (mm)	120
Speed (r/min)	600
Series turns per phase	6
Rated RMS current (A)	10

torque and torque ripple are most influenced by two key parameters: the thickness of the stator PM L_{PM} and the pole arc θ_{PM}.

Figure 5 shows the response surface analysis of torque and torque ripple with respect to two key parameters: stator PM thickness L_{PM} and pole arc angle θ_{PM}. It reveals that both parameters have a significant impact on the output performance. This is because they directly influence the air-gap flux density, which in turn affects the average torque and torque ripple.

Similarly, for the proposed DPFRM, Fig. 4(b) illustrates the key structural parameters, among which sensitivity analysis identifies three critical variables influencing the output torque and ripple: the stator-side sandwich Halbach PM thickness PM_t, and the arc angles θ_t and θ_{PM}, which define the stator-rotor PM coverage region. These parameters are then used for

response surface analysis to investigate their effects on torque and ripple, as illustrated in Figs. 6–8.

Due to the mutual constraints and influence between the parameters, it is necessary to perform the global optimization and select the appropriate points.

Figure 9 illustrates the distribution of candidate points for both the FRM and DPFRM. As shown in Fig. 9(a), the selected optimal point offers a relatively low torque ripple while maintaining a high average torque. In this region, torque increases slowly, but torque ripple grows rapidly with further improvement in torque. To achieve a practical trade-off between torque output and ripple suppression, the selected point is located just before this sharp rise. This balance is favorable for stable operation and suits applications requiring smoother torque performance. The final design parameters for both topologies are summarized in Table 3.

TABLE 3. Optimized parameters.

Parameters	FRM	DPFRM
θ_{PM} (deg)	9.39	8.40
θ_t (deg)	4.86	5.50
L_{PM} (mm)	4.64	
PM_t (mm)	5.63	6.00
L_t (mm)		6.0
R_{so} (mm)	70.06	75.00
PM volume (cm^3)	13.40	19.62

4. COMPARISON OF NO-LOAD PERFORMANCE

4.1. Field Distribution Plots

Figure 10 illustrates the magnetic flux distribution of the FRM and DPFRM under no-load conditions. It can be observed that the DPFRM exhibits higher core and PM utilization. This is attributed to the consequent-pole structures on both the stator and rotor sides, which help reduce magnetic reluctance. In addition, the Halbach arrays guide the magnetic flux more effectively, contributing to higher torque output and reduced torque ripple.

Figure 10 illustrates the magnetic flux distribution of the FRM and DPFRM under no-load conditions. It can be observed that the DPFRM exhibits higher core and PM utilization. This is attributed to the consequent-pole structures on both the stator and rotor sides, which help reduce magnetic reluctance. In addition, the Halbach ar-rays guide the magnetic flux more effectively, contributing to higher torque output and reduced torque ripple.

4.2. Back-EMF

Figure 11 presents the back-EMF waveforms and harmonic spectra for both FRM and DPFRM. The DPFRM achieves a peak back-EMF of 79.59 V, marking a 36.63% increase over the 58.25 V observed in the conventional FRM. The harmonic analysis shows that the DPFRM not only exhibits a higher funda-
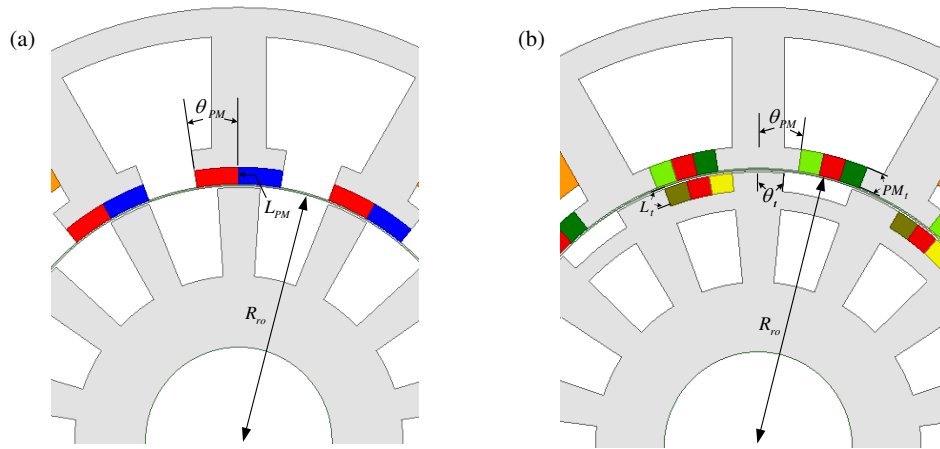
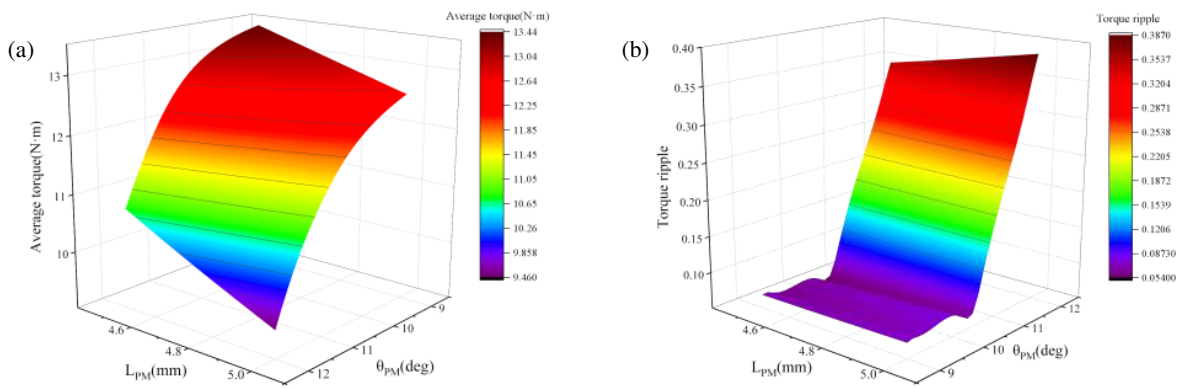**FIGURE 4**. Key structural parameters. (a) FRM. (b) DPFRM.

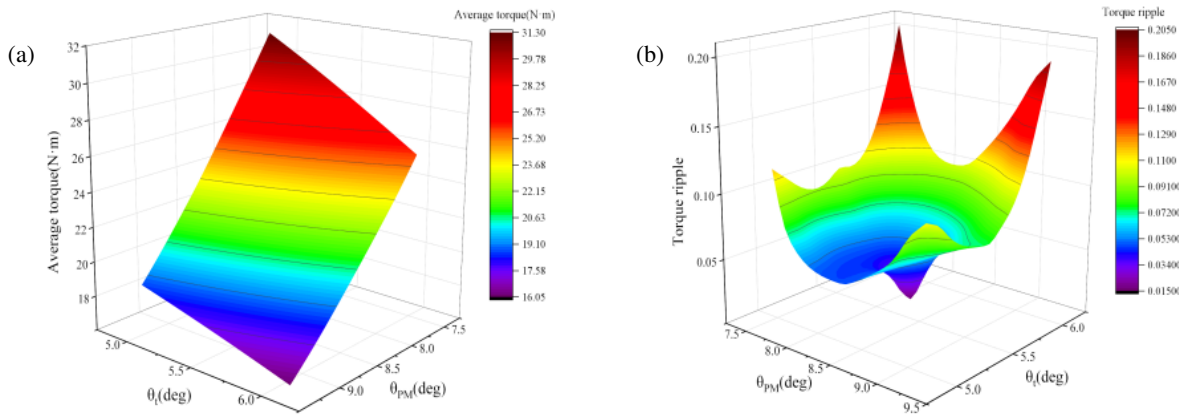**FIGURE 5**. Torque performance changing versus L_{PM} and θ_{PM} of FRM. (a) Average torque. (b) Torque ripple.

FIGURE 6. Torque performance changing versus θ_t and θ_{PM} of DPFRM. (a) Average torque. (b) Torque ripple.

mental component, which directly contributes to greater torque, but also contains more working harmonics.

4.3. Cogging Torque

Figure 12 illustrates the comparison of cogging torque between the FRM and DPFRM. It can be observed that the DPFRM exhibits a higher cogging torque than the FRM. This increase is primarily caused by the dual-layer PM configuration, which

introduces additional magnetic interactions — specifically between the stator PMs and rotor slots, as well as between the rotor PMs and stator slots.

5. COMPARISON OF LOAD PERFORMANCE

5.1. Rated Load

Figure 13 shows the excitation current waveform applied in the finite element simulations. A three-phase sinusoidal current
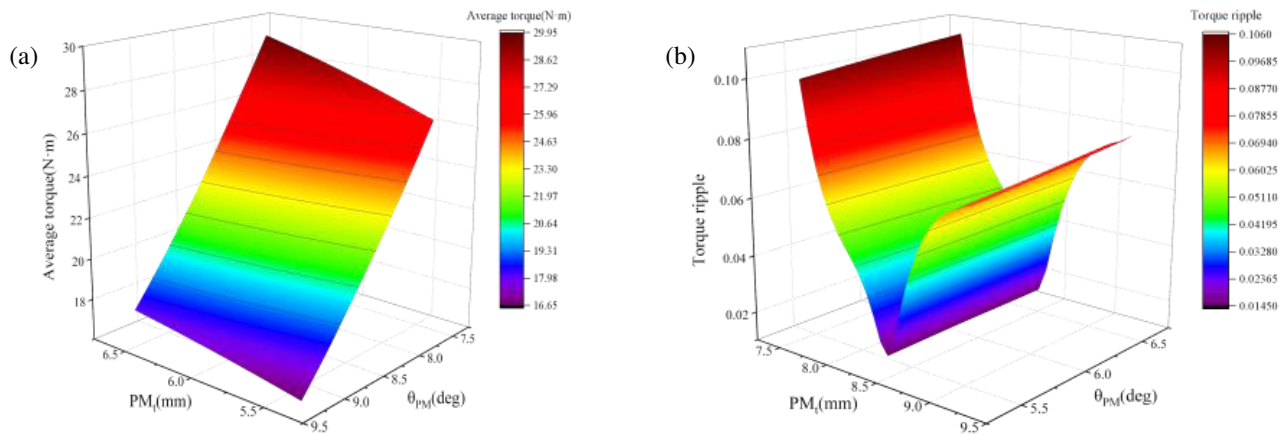
FIGURE 7. Torque performance changing versus PM_t and θ_{PM} of DPFRM. (a) Average torque. (b) Torque ripple.
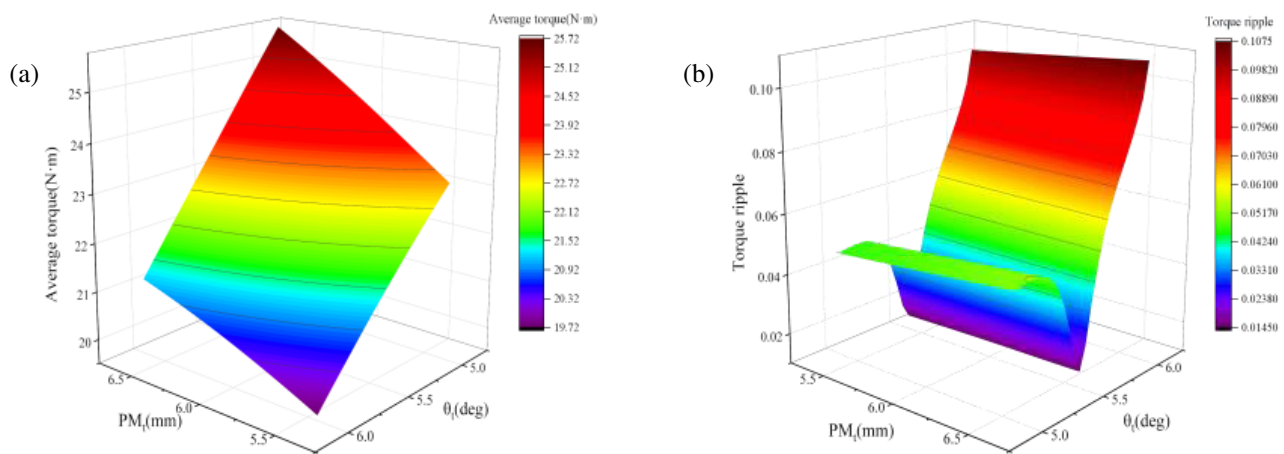

FIGURE 8. Torque performance changing versus PM_t and θ_t of DPFRM. (a) Average torque. (b) Torque ripple.
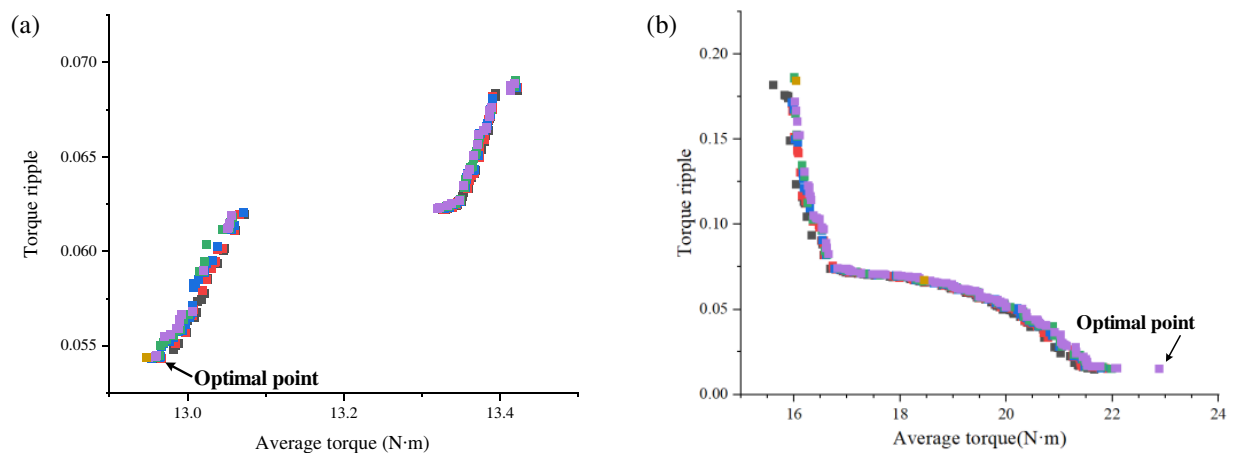

FIGURE 9. Optimization result. (a) FRM. (b) DPFRM.

with a rated root-mean-square (RMS) value of 10 A is used as the excitation for both machines.

Figure 14 compares the load characteristics and torque density of the FRM and DPFRM. Under the same sinusoidal current excitation, the FRM produces an average torque of 12.76 N · m with a torque ripple of 3.99%, while the DPFRM achieves a higher average torque of 22.61 N · m and a lower ripple of just 1.61%.

Considering the difference in PM usage between the two designs, their torque densities are compared under various current
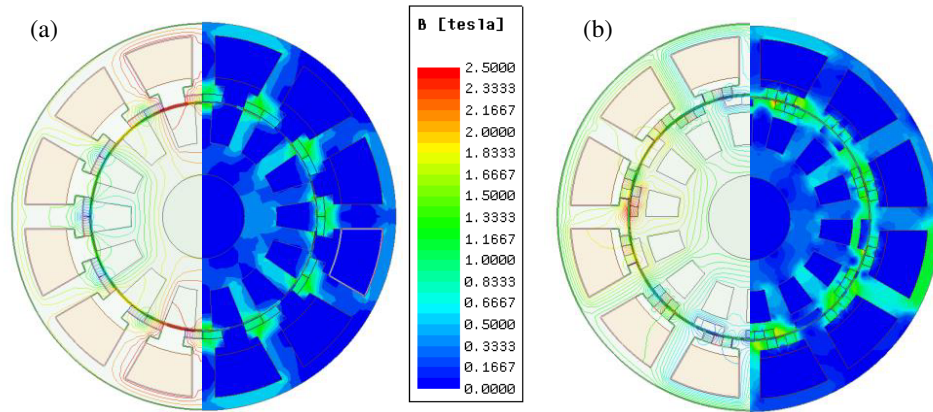
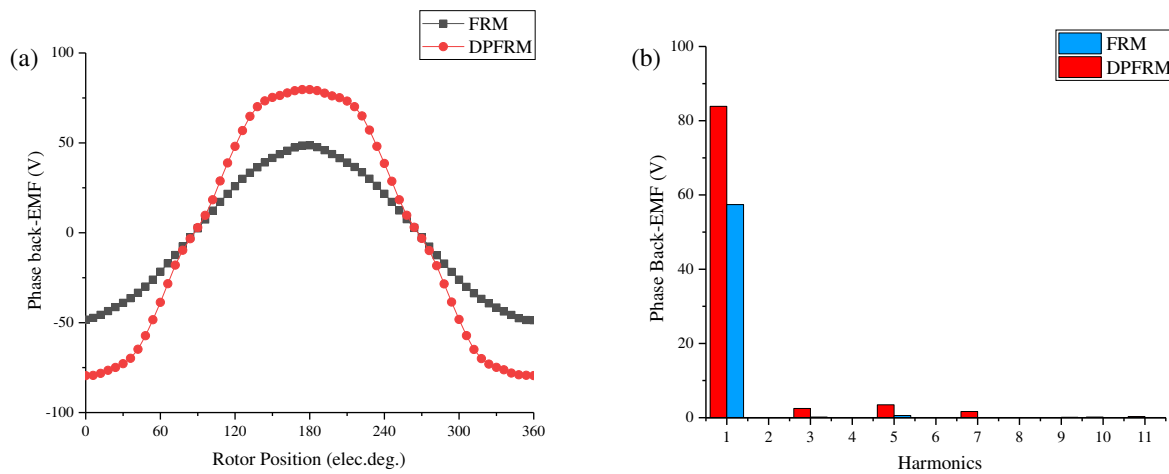FIGURE 10. Field distribution plots. (a) FRM. (b) DPFRM.

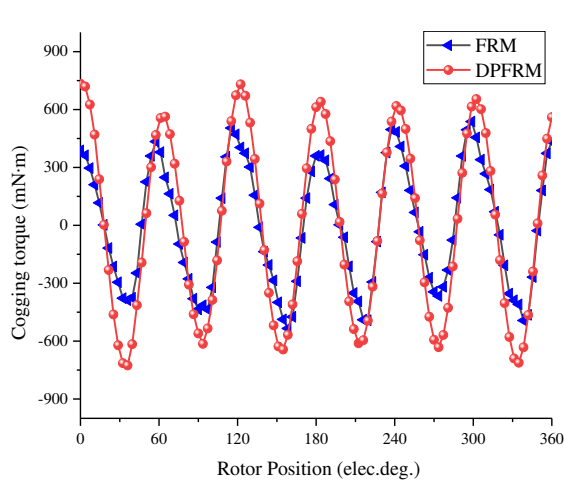FIGURE 11. Back-EMF. (a) Waveform. (b) Harmonic spectra.

FIGURE 12. Cogging torque of FRM and DPFRM.

FIGURE 13. Sinusoidal current excitation waveform used in the simulation (RMS = 10 A).

levels. When the excitation current is below 6 A, the DPFRM shows more than a 100% increase in torque density, with a peak improvement of 408.17% at 2 A. Even at 10 A, the torque density is still 20.96% higher, highlighting the DPFRM's efficiency under low-current conditions.
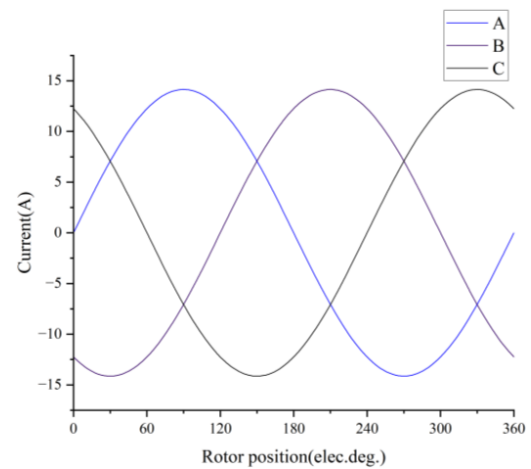
5.2. Overload Capability

Figure 15 shows the average torque of both topologies under different current excitations. The DPFRM delivers higher torque at low current levels, demonstrating better efficiency in light-load conditions. However, as current increases, its torque growth slows down due to stronger magnetic saturation effects.
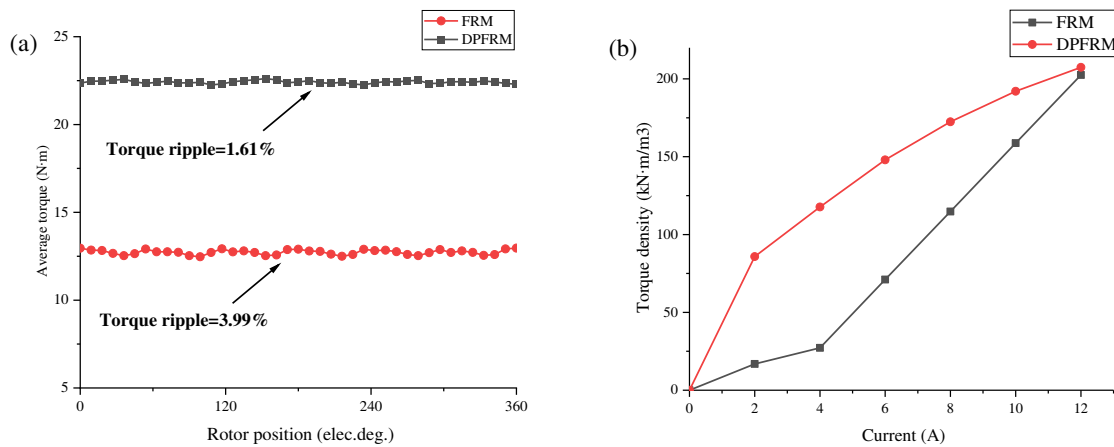
FIGURE 14. Performance comparison. (a) Load characteristics. (b) Torque density.

6. CONCLUSION

In this paper, a modified DPFRM with Halbach arrays and a reduced rotor PM layout is proposed to enhance electromagnetic performance and improve PM utilization. Based on the FEA, the main conclusions are drawn as follows:

1) Compared with the conventional FRM, the proposed DPFRM achieves a 36.63% increase in back-EMF and a 75.24% increase in average torque. It also exhibits improved torque density under low current conditions.

2) The application of Halbach arrays in both stator and rotor sides forms a consequent-pole structure, which effectively reduces magnetic flux leakage. Meanwhile, the torque ripple is significantly reduced from 3.99% to 1.61%, improving the output smoothness of the machine.

3) The proposed structure offers better electromagnetic performance, but it may lead to increased manufacturing complexity and a higher risk of magnetic saturation, which should be considered in future structural or material optimizations.

4) With its notably low torque ripple and improved torque density at low current, the proposed DPFRM shows strong potential for precision drive applications and compact direct-drive systems where smooth torque and high efficiency are required.

FIGURE 15. Torque current curves of the FRM and DPFRM.

REFERENCES

[1] Zhu, Z.-Q. and D. Howe, "Electrical machines and drives for electric, hybrid, and fuel cell vehicles," *Proceedings of the IEEE*, Vol. 95, No. 4, 746–765, Apr. 2007.

[2] Shi, Z., X. Sun, Z. Yang, Y. Cai, G. Lei, J. Zhu, and C. H. T. Lee, "Design optimization of a spoke-type axial-flux PM machine for in-wheel drive operation," *IEEE Transactions on Transportation Electrification*, Vol. 10, No. 2, 3770–3781, Jun. 2024.
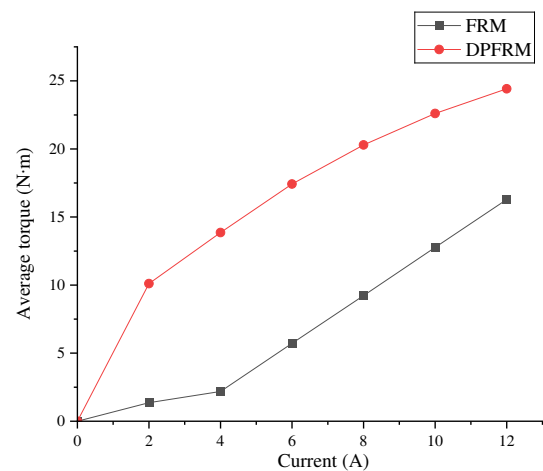
[3] Sun, X., N. Xu, and M. Yao, "Sequential subspace optimization design of a dual three-phase permanent magnet synchronous hub motor based on NSGA III," *IEEE Transactions on Transportation Electrification*, Vol. 9, No. 1, 622–630, Mar. 2023.

[4] Shi, Z., X. Sun, G. Lei, X. Tian, Y. Guo, and J. Zhu, "Multiobjective optimization of a five-phase bearingless permanent magnet motor considering winding area," *IEEE/ASME Transactions on Mechatronics*, Vol. 27, No. 5, 2657–2666, Oct. 2022.

[5] Zou, T., D. Li, R. Qu, and D. Jiang, "Performance comparison of surface and spoke-type flux-modulation machines with different pole ratios," *IEEE Transactions on Magnetics*, Vol. 53, No. 6, 1–5, Jun. 2017.

[6] Wu, Z., Z.-Q. Zhu, and H. Zhan, "Comparative analysis of partitioned stator flux reversal PM machine and magnetically geared machine operating in stator-PM and rotor-PM modes," *IEEE Transactions on Energy Conversion*, Vol. 32, No. 3, 903–917, Sep. 2017.

[7] Chau, K. T., C. C. Chan, and C. Liu, "Overview of permanent-magnet brushless drives for electric and hybrid electric vehicles," *IEEE Transactions on Industrial Electronics*, Vol. 55, No. 6, 2246–2257, Jun. 2008.

[8] Cheng, M., W. Hua, J. Zhang, and W. Zhao, "Overview of stator-permanent magnet brushless machines," *IEEE Transactions on Industrial Electronics*, Vol. 58, No. 11, 5087–5101, Nov. 2011.

[9] Cheng, H., J. Cui, C. Peng, J. Chu, J. Zhou, and Z. Ye, "Electromagnetic characteristics analysis and torque ripple reduction for doubly salient PM machine," *IEEE Transactions on Energy Conversion*, Vol. 38, No. 3, 1659–1668, Sep. 2023.

[10] Zhu, X. and W. Huang, "Investigation of five-phase flux-switching permanent magnet machines for EV and HEV applications," *IEEE Transactions on Industry Applications*, Vol. 60, No. 1, 1071–1082, Jan.–Feb. 2024.

[11] Zheng, Y., W. Xiang, H. Xu, P. Tan, and Y. Fang, "Analysis of a flux reversal machine with consequent-pole evenly distributed PM," *IEEE Transactions on Industry Applications*, Vol. 60, No. 1, 4–11, Jan.–Feb. 2024.

[12] Gao, Y., R. Qu, D. Li, and J. Li, "Torque performance analysis of three-phase flux reversal machines," *IEEE Transactions on Industry Applications*, Vol. 53, No. 3, 2110–2119, May–Jun. 2017.

[13] Yang, K., F. Zhao, Y. Wang, and Z. Bao, "Consequent-pole flux reversal permanent magnet machine with halbach array magnets in rotor slot," *IEEE Transactions on Magnetics*, Vol. 57, No. 2, 1–5, Feb. 2021.

[14] Gao, Y., R. Qu, D. Li, J. Li, and G. Zhou, "Consequent-pole flux-reversal permanent-magnet machine for electric vehicle propulsion," *IEEE Transactions on Applied Superconductivity*, Vol. 26, No. 4, 1–5, Jun. 2016.

[15] Wei, F., Z. Q. Zhu, H. Qu, L. Yan, and J. Qi, "New dual-PM spoke-type flux-reversal machines for direct-drive applications,"

IEEE Transactions on Industry Applications, Vol. 58, No. 5, 6190–6202, Sep.–Oct. 2022.

[16] Gao, Y., T. Kosaka, Y. Liu, M. Doppelbauer, and R. Qu, "Comparative analysis of double flux modulation permanent magnet machines with different stator PM arrangements," *IEEE Transactions on Industry Applications*, Vol. 58, No. 2, 1941–1951, Mar.–Apr. 2022.

[17] Aslani, B., S. E. Abdollahi, and S. A. Gholamian, "A novel dual-PM flux reversal machine with halbach array magnets in stator slots," in *2023 3rd International Conference on Electrical Machines and Drives (ICEMD)*, 1–5, Tehran, Islamic Republic of Iran, 2023.

[18] Wei, F., Z. Q. Zhu, Y. Zheng, and H. Xu, "Comparative study of stator-PM and dual-PM consequent-pole hybrid excited flux-reversal machines," in *2022 25th International Conference on Electrical Machines and Systems (ICEMS)*, 1–5, Chiang Mai, Thailand, 2022.

[19] Sun, P., S. Jia, D. Yang, D. Liang, and Z. Luo, "Design and comparative analysis of dual winding dual magnet machines with different PM arrangements," *IEEE Transactions on Industry Applications*, Vol. 61, No. 1, 151–160, Jan.–Feb. 2025.

[20] Wang, Q., S. Niu, and L. Yang, "Design optimization and comparative study of novel dual-PM excited machines," *IEEE Transactions on Industrial Electronics*, Vol. 64, No. 12, 9924–9933, Dec. 2017.